AIAA SciTech Forum
11–15 & 19–21 January 2021, VIRTUAL EVENT
AIAA Scitech 2021 Forum

10.2514/6.2021-1350

Stochastic microstructural analysis of ceramic matrix composites using a high-fidelity multiscale framework

K. H. Khafagy[1], K. R. Venkatesan[1], K. Balusu[2], S. Datta[2] and A. Chattopadhyay[3]
School for Engineering of Matter, Transport, and Energy, Arizona State University, Tempe, AZ, 85281, USA

This paper presents a high-fidelity multiscale framework to simulate the mechanical behavior of ceramic matrix composites (CMCs), accounting for the complex micromorphology captured using detailed material characterization. First, high-resolution micrographs are obtained for the specific carbon fiber silicon-carbide-nitride matrix (C/SiNC) CMC to characterize the variability of the architectural features and manufacturing-induced defects at the microscale. An image processing algorithm is then used to precisely estimate the size and distribution of all subscale features and defects from the micrographs. The information is then used to generate a three-dimensional stochastic representative volume element (SRVE) to reconstruct microscale constituents accounting for the variability. Last, the generated SRVEs are simulated using the high-fidelity generalized method of cells (HFGMC) micromechanics theory to investigate the effects of defects on the elastic properties of C/SiNC CMCs.

I- Introduction

Ceramic matrix composites (CMCs) possess characteristics such as lightweight, high strength and toughness, high-temperature capabilities, and controlled failure under loading. They are used in various applications involving harsh environments such as engine hot-section components [1-2]. However, the inherent capabilities of CMCs are not fully exploited due to a lack of complete understanding of the material performance under critical mechanical and environmental loading environments. Property scatter is notionally caused by variability in processing related parameters such as constituent volume fractions, tow spacing, shape and size, porosity, etc. The size, distribution, and morphology of defects such as voids at different length scale significantly impact their strength and toughness [3- 4], thus highlighting the need for exhaustive material characterization and quantification of these defects.

Several authors have quantified the effects of defects in CMCs using experimental microscopy techniques. Gowayed et al. provided an overview of flaws in SiC/SiNC CMCs using optical microscopy; the authors categorized the flaws into different categories such as inter- and intrayarn defects [5]. A simple analytical model was also used to investigate the effects of material defects on the elastic properties of two systems of SiC/SiC and one oxide/oxide CMCs. The elastic properties were shown to deteriorate with increasing volume fraction (VF) of defects. Puglia et al. provided an overview of the quantification of defects in the T300C/SiC CMC material system [6]. Santhosh et al. used thermography scanning images to characterize and quantify porosity in CG-Nicalon^{TM}/SiNC CMCs [7]. More recently, they used spheroidal inclusions with a micromechanics-based progressive damage model to predict the effects of porosity on the elastic properties for CG-Nicalon/SiNC CMCs [8]. Their results showed a more significant knockdown in the through-thickness modulus compared to the in-plane modulus.

While analytical and semi-empirical models can predict the homogenized properties of CMCs, they cannot capture the critical load transfer characteristics and damage mechanisms at lower length scales, which can lead to unreliable strength and life cycle predictions. CMCs typically exhibit damage at multiple length scales in the form of intertow and intratow matrix microcracks, fiber-matrix interfacial debonding, and progressive fiber failure. Moreover, defects in the individual constituents create additional complexities in the accurate modeling and analysis of

[1] Graduate Research Associate, School for Engineering of Matter, Transport, and Energy, ASU
[2] Postdoctoral Research Associate, School for Engineering of Matter, Transport, and Energy, ASU
[3] Regents' Professor & Ira. A Fulton Professor of Mechanical and Aerospace Engineering, School for Engineering of Matter, Transport, and Energy, ASU, AIAA Fellow

CMCs. Therefore, it is essential to develop accurate models linking the constituent properties and subscale features to CMC response under thermomechanical loading.

To date, there is no multiscale framework that can accurately capture the uncertainty in the predicted response while accounting for the architectural features and the actual shape and distribution of defects in CMCs. In addition to accurate physics-based models, such a methodology will heavily rely on systematic consideration of the most relevant, scale-dependent variability and its propagation across the length scales within the multiscale modeling framework. Therefore, it is essential to define statistically equivalent representative volume elements (SRVEs) that can precisely capture the microstructural variability and the processing-induced flaws. Although large-sized SRVEs can help capture the critical subscale features and variability, the resulting computational cost limits their use within a multiscale framework. As a result, existing approaches are limited to idealized microscale RVEs [9-11], making it difficult to accurately capture the effects of defects and variability at higher length scales.

In this work, a high-fidelity multiscale framework is used to capture the effects of microstructural variability on the effective response of CMCs. First, material characterization studies are conducted on a carbon fiber silicon-carbide-nitride matrix (C/SiNC) CMC to investigate the architectural and geometric variability and manufacturing flaws at multiple length scales. This is particularly important since the specific CMC's microscopy data is not readily available in the published literature. A generic three-dimensional (3D) microstructure generation algorithm is developed to explicitly model the individual constituent phases and defects based on a range of characterization data. A recently developed reformulated high-fidelity generalized method of cells (HFGMC) theory [12] is used to simulate the 3D microscale SRVEs and investigate the stochasticity in the predicted output properties of interest. The reformulated theory requires a significantly reduced number of unknowns to solve the SRVE boundary value problem, resulting in decreased computational cost. The methodology is also integrated with existing parallelization schemes and high-performance computing (HPC) architectures to simulate large-sized SRVEs, with significantly increased computational efficiency. This framework is then used to investigate the effects of intratow porosity defects on the predicted elastic properties of C/SiNC CMCs.

II-Multiscale structure and defects characterization

In a previous investigation by the authors [13], the defects in C/SiNC CMCs were characterized using several microscopy and image processing techniques. Microscopy techniques such as scanning electron microscope (SEM) and confocal laser scanning microscope (LSM) were used to quantify flaws such as interlaminar debonding, denuded matrix defects, open or intertow porosity, shrinkage cracks, and intratow porosity in the as-received coupons. Figure 1 illustrates the material features and flaws obtained from the LSM at the micro- and mesoscales. Mesoscale defects such as open porosity and denuded matrix (cross over defects) "i" are shown in Fig. 1(a). Open porosity defects that have a favored direction (transverse) and shape (elliptical) act as a bridging mechanism between adjacent tows; see "ii" in Fig 1(b). At the microscale, intratow porosity "iii", which has favored location, distribution, and shape, is shown in Fig. 1(c). High-resolution SEM micrographs were used for further characterization of the variability in material architecture and as-produced flaws.

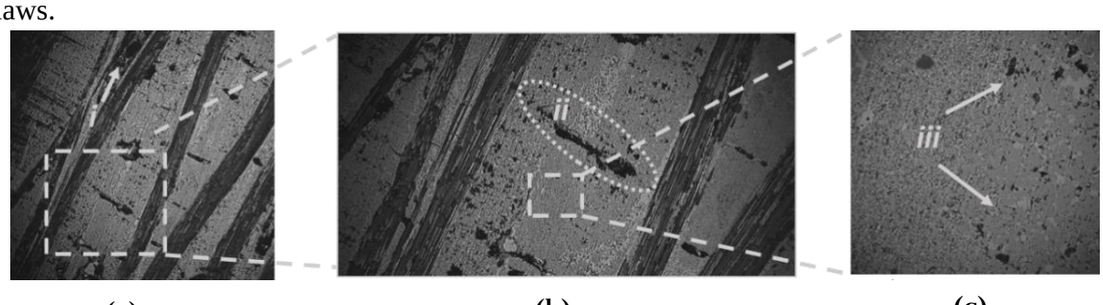

Fig. 1. C/SiNC CMC micrographs: (a) Denuded matrix defects at 5x magnification; (b) open porosity defects at 10x magnification; (c) intratow porosity defects at 50x magnification

Different ceramic phases such as SiNC matrix and other ceramic particles were observed; see (*a) and (*b) in Fig. 2(a). Fiber arrangement, size, misalignment, and even distributions of the ceramic phases in intra- and intertow regions can be seen in Fig. 2(b). Figure 2(c) shows an example of a fiber-matrix interface damage “c” and Si-rich ceramic phases in intratow regions (*d). Furthermore, it is possible to estimate the fiber circular cross-section and hexagonal fiber close packing structure from the micrographs in Fig. 2.

An image processing algorithm based on the image segmentation process was used to identify constituent volumes and defects from several microscopy graphs and quantify the uncertainty in architectural parameters such as fiber size and volume fraction, inter- and intratow spacing, and inter- and intratow void size, distribution and volume fractions. The obtained data was then used to build probability distribution functions (PDFs) for the corresponding input parameters. The readers are referred to [13] for additional details.

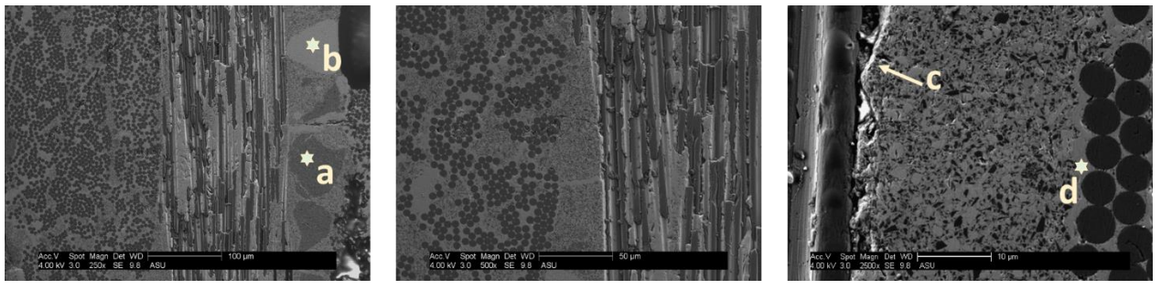

(a) **(b)** **(c)**

Fig. 2. C/SiNC CMC micrographs: (a) different ceramic phases in intertow regions “*a” and “*b”; (b) fibers arrangement, size, and misalignment; (c) matrix-fiber interface damage “c” and Si-rich zones “*d”

III-A three-dimensional stochastic RVE generation

The detailed variability results are used to estimate key properties such as inter- and intratow porosity VF, fiber VF, fiber radii and intratow spacing distributions, and average tow size, and the information is used as inputs to generate the C/SiNC CMC SRVEs [13]. At the macroscale, the generated SRVE is assumed as a material point with periodic boundary conditions (PBCs). Therefore, fiber misalignment is neglected in the current work. The algorithm also models all the composite constituents, such as fiber, matrix, interphase layers, and inter- and intratow defects. Accurate representations of porosity in the generated SRVEs, considering their favored location, distribution, direction, shape, and VF, are considered. For instance, a geometry of eight fibers surrounded by a matrix in a domain size of 100 x 100 x 60 structured orthogonal grid is shown in Fig. 3. Figure 3(a) shows a 2D view of the SRVE where the fiber arrangements, intratow spacing, and the PBCs are evident across the four boundaries. Figure 3(b) shows a 3D view of the fiber in the SRVE, where fiber misalignments are neglected, and fiber periodicity can easily be detected across the SRVE corners. Figure (4) shows the distribution and shape of intratow voids, based on intratow voids characterization variability results. From the characterization results, the favored locations of intratow voids are located on the fiber/matrix interfaces, between the fibers within fiber close-packing regions, and randomly distributed in the matrix domain [13]. The generated intratow voids show these favored locations such as in fiber close-packing regions (see “i” in Fig. 4(a)), randomly selected voids in the matrix regions (see “ii” in Fig. 4(a)), and void coalescence at the fiber-matrix interface (see “iii” in Fig. 4(b)). Note that only the matrix regions are affected by the intratow voids. The resulting SRVE shows excellent correlations with the C/SiNC CMC micrographs.

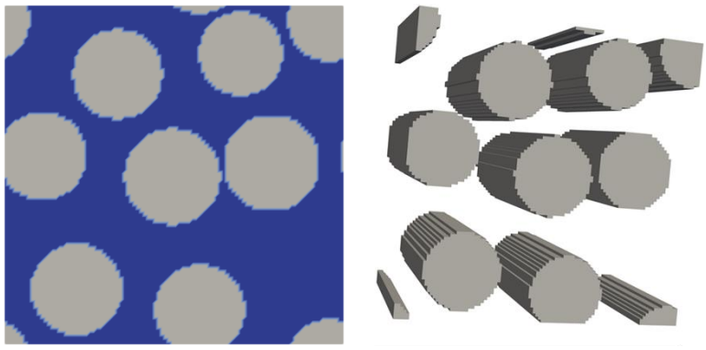

(a) **(b)**

Fig. 3 Example of an SRVE with 100x100x60 grid size domain and eight fibers surrounded by matrix, (a) a two-dimensional view of the generated SRVE, and (b) a three-dimensional view of the generated SRVE

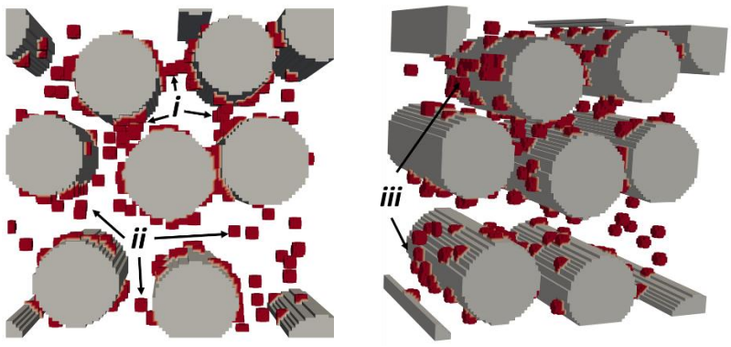

(a) **(b)**

Fig. 4 Example of introducing intratow voids in the generated SRVE with favored location, distribution, and shape (a) a 2D view showing voids in fiber close-packing regions "i" and randomly distributed in the matrix domain "ii", and (b) a 3D view showing void coalescence at the fiber-matrix interface "iii"

IV-High fidelity generalized method of cells (HFGMC)

The elastic simulations of the microscale SRVEs are carried out using an efficient implementation of the HFGMC theory developed by the authors [12]. The HFGMC employs second-order displacement field expressions instead of the first-order displacement field expressions in the generalized method of cells (GMC), thereby accounting for the normal-shear coupling and resulting in an accurate simulation of stress and strain fields within the SRVE [14].

In the HFGMC formulation, the material is represented by a triply periodic repeated volume element (RVE), as shown in Fig. 5(a). The RVE is discretized into cuboid-shaped volumes, termed as subcells, each with a specific constituent material. Fig. 5(b) shows each subcell is assigned an index (α, β, γ), where the indices $\alpha = 1,2 \dots, N_\alpha$, $\beta = 1,2 \dots, N_\beta$, and $\gamma = 1,2 \dots, N_\gamma$ span the RVE along the three orthogonal axes, y_1, y_2 *and* y_3. The local subcell strain components are given as

$$\varepsilon_{ij} = \bar{\varepsilon}_{ij}(\boldsymbol{x}) + \varepsilon'_{ij}(\boldsymbol{x}, \boldsymbol{y}) \tag{1}$$

where $\bar{\varepsilon}_{ij}(\boldsymbol{x})$ is the homogenized/effective strain field at a macroscopic point $\boldsymbol{x}$, and $\varepsilon'_{ij}(\boldsymbol{x}, \boldsymbol{y})$ is the fluctuating strain field at the microscopic point $\boldsymbol{y}$. The fluctuating strain field is derived from the fluctuating subcell displacement field approximated using second-order polynomial expansion as:

$$u'^{(\alpha,\beta,\gamma)}_i = W^{(\alpha,\beta,\gamma)}_{i(000)} + \bar{y}_1^{(\alpha)} W^{(\alpha,\beta,\gamma)}_{i(100)} + + \bar{y}_2^{(\beta)} W^{(\alpha,\beta,\gamma)}_{i(010)} + \bar{y}_3^{(\gamma)} W^{(\alpha,\beta,\gamma)}_{i(001)} +$$

$$\frac{1}{2}\left(3\bar{y}_1^{(\alpha)2} - \frac{h_\alpha^2}{4}\right) W^{(\alpha,\beta,\gamma)}_{i(200)} + \frac{1}{2}\left(3\bar{y}_2^{(\beta)2} - \frac{h_\beta^2}{4}\right) W^{(\alpha,\beta,\gamma)}_{i(020)} + \frac{1}{2}\left(3\bar{y}_3^{(\gamma)2} - \frac{h_\gamma^2}{4}\right) W^{(\alpha,\beta,\gamma)}_{i(002)} \tag{2}$$

where $W_{i(lmn)}^{(\alpha,\beta,\gamma)}$ are the unknown micro-variables associated with each subcell, $\bar{y}_1{}^{(\alpha)}$, $\bar{y}_2{}^{(\beta)}$and $\bar{y}_3{}^{(\gamma)}$ represent the local coordinates of the subcell, and h_α, h_β and h_γ are the subcell dimensions.

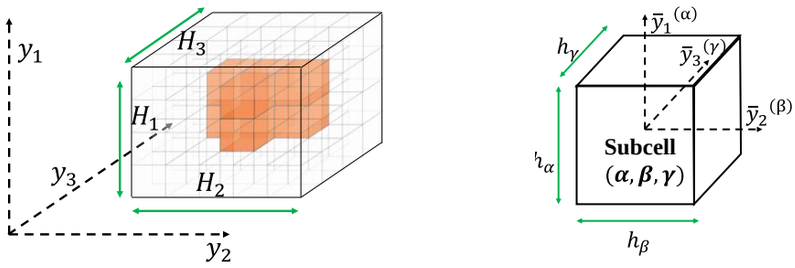

(a) **(b)**

Fig. 5 (a) A triply periodic repeated volume element (RVE) representing the microstructure and (b) one of its subcells with indices (α,β,γ).

In the efficient reformulation [12,15], the micro variables are replaced by the surface averaged displacement vectors of each subcell as unknowns. The replacement is accomplished by enforcing the continuity of surface averaged displacements at the boundary between every subcell. Additionally, PBC is imposed on the subcell surfaces and at the edge of the SRVE. This reformulation reduces the number of unknowns per subcells from 21 to 9, thereby significantly improving computational efficiency. The necessary continuity and boundary conditions lead to a system of linear equations given by

$$\boldsymbol{KU} = \boldsymbol{f} \tag{3}$$

where the matrix $\boldsymbol{K}$, and vector $\boldsymbol{f}$ are a function of the constituent elastic material properties and the effective SRVE strains, and $\boldsymbol{U}$ is the vector of the unknown surface averaged displacements. In the efficient implementation of the HFGMC, the matrix $\boldsymbol{K}$, and vector $\boldsymbol{f}$ are represented using the sparse matrix representation. The solution for $\boldsymbol{U}$ vector is found using linear equation solvers for sparse matrices. Sparse matrix implementation significantly improves computational efficiency, making it possible to analyze complex microstructures at high mesh resolutions. Further reduction in computation time is made possible using parallel processors in a high-performance computer (HPC). More details on the sparse matrix implementation and parallel processing integration can be found in Ref. [12].

The components of the homogenized stress field $\bar{\boldsymbol{\sigma}}$ of the SRVE are determined by performing a volume average of the local subcell stress field. The homogenized stiffness matrix $\boldsymbol{C}^*$ of the SRVE can then be estimated from the global constitutive relationship given by

$$\bar{\boldsymbol{\sigma}} = \boldsymbol{C}^*\bar{\boldsymbol{\varepsilon}} \tag{4}$$

Six independent elastic strain computations are required to estimate the homogenized stiffness matrix. In the first elastic computation, the macroscopic strain vector $\bar{\varepsilon}$ is chosen such that the first component $(\bar{\varepsilon}_{11})$ has a value of one, and the other components are zeros. The resulting macroscopic stress vector is the first column of the homogenized stiffness matrix. The other five columns of the stiffness matrix are estimated using a similar manner. More details on the formulation and the estimation of effective composite properties can be found in [16].

V- Microstructural analysis

In this work, 400 stochastic SRVEs, each generated with 13 fibers, ~49.59 % fiber VF, and a domain grid size of 105x105x13, were used. The first 100 SRVEs accounted for 0 % intratow porosity VF while the remaining 300 accounted for 1%, 2%, and 3% porosity VFs. The domain grid size of the SRVE without porosity was adjusted as 105x105x3 to save the computational cost. The elastic properties of the individual microscale constituents are listed in Table (1). Figure 6(a) shows the effects of 3% VF of intratow porosity on the longitudinal elastic modulus of the material, where the mean value of the longitudinal modulus deteriorates by ~8%. The effects of 3% VF of intratow porosity on the transverse Young's modulus are shown in Fig. 6(b), where the mean value decreased by 14.92%. The effect of intratow porosity is more significant along the transverse direction due to the void's location and distribution and its abundant presence within the matrix constituent.

Table 1. C/SiC CMC elastic properties [17- 18]

	E_{11} (GPa)	E_{22} (GPa)	ν_{12}	ν_{23}	G_{12} (GPa)
T300 Carbon fibers	231	22	0.3	0.35	15
SiC Matrix	415	415	0.17	0.17	177.35

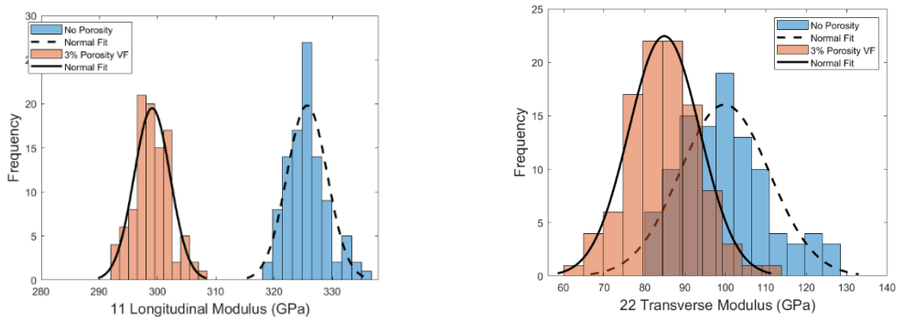

(a) **(b)**

Fig. 6 Effects of 3% VF of intratow porosity on the elastic moduli of the material; (a) longitudinal Young's modulus; (b) transverse Young's modulus

Figure (7) shows the effect of intratow porosity with different VF (1%, 2%, and 3%) on various elastic moduli. Figure 7(a) shows the decrease in mean longitudinal Young's modulus values with increased porosity VF. The error bar at each VF indicates the predicted standard deviation from stochastic HFGMC simulations. The transverse Young's modulus also decreases with an increase in porosity VF, as shown in Fig. 7(b). Likewise, the transverse shear modulus decreased by 15.72 %, with an increase in the porosity VF, as shown in Fig. 7(c).

Consequently, the effect of increasing porosity VF is more dominant in the out-of-plane direction than in the in-plane direction. Moreover, the transverse normal and shear moduli have a larger standard deviation compared to the longitudinal modulus. This can be attributed to the location and distribution of the more prominent voids near the fiber-matrix interface. Since the interface plays a crucial role in the load transfer characteristics, the effect of porosity on the modulus is more significant along the transverse normal and shear direction. While the present effort is limited to elastic analysis, the incorporation of damage models in future studies will allow for microcracks to initiate in the matrix regions with high-stress concentrations due to such porosity defects.

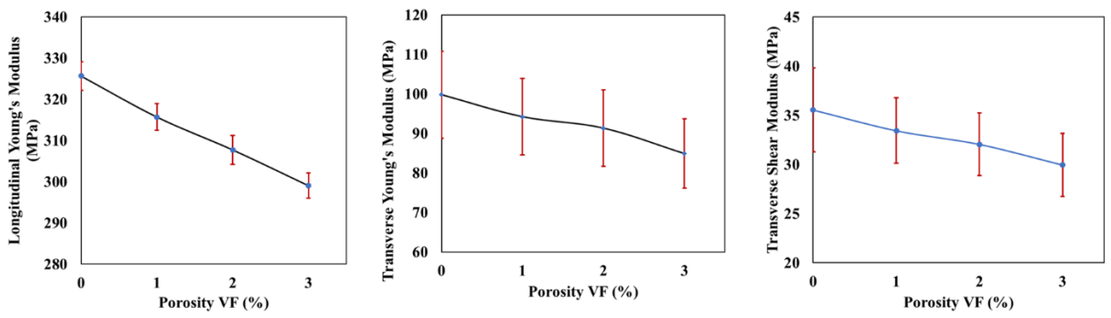

(a) **(b)** **(c)**

Fig. 7 Effects of intratow porosity density on the elastic moduli of the material such as; (a) longitudinal Young's modulus; (b) transverse shear modulus; (c) transverse Young's modulus

VI-Conclusions

In this work, a high-fidelity multiscale framework was used to predict the mechanical properties of ceramic matrix composites (CMCs) while accounting for the complex micromorphology captured from a detailed material characterization study. High-resolution micrographs obtained from scanning electron microscopy (SEM) and laser scanning microscopy (LSM) techniques were used to investigate the defects and variability in C/SiNC CMCs. Defects such as intratow porosity, intertow open porosity, and mesoscale defects such as denuded matrix, interlaminar separation were observed.

A three-dimensional stochastic representative volume element (SRVE) was generated to accurately represent the architectural features and defects based on the microscale characterization results. The developed SRVE precisely accounts for the favored location of defects and their distribution, shape, and volume fractions. The generated SRVEs show an excellent match with the experimental micrographs. Last, a parallelized version of the reformulated high-fidelity generalized method of cells (HFGMC) was used to efficiently simulate the SRVEs and investigate the effects of microscale (intratow) defects on the elastic properties of C/SiNC CMCs. The deterioration in elastic properties was prominent in the out of plane direction due to the location and distribution of intratow porosity defects primarily near the fiber-matrix interface region.

Acknowledgments

The research reported in this paper is supported in part by the Air Force Office of Scientific Research (Grant FA9550-18-1-00129, Project Manager: Jaimie Tiley), and the Department of Energy (Grant DE-FOA-0001993, Project Manager: Matthew F. Adams).

References

[1] F.W.Zok, Ceramic-matrix composites enable revolutionary gains in turbine engine efficiency, Am. Ceram. Soc. Bull. 95 (2016) 22 28. https://ceramics.org/wp-content/bulletin/2016/junejuly16/JuneJuly16Bulletin-ceramic-matrix-composites.pdf.

[2] P.G. Valentine, P.R. Gradl, Extreme-temperature carbon- And ceramic-matrix composite nozzle extensions for liquid rocket engines, in: Proc. Int. Astronaut. Congr. IAC, 2019: pp. 21–25. https://ntrs.nasa.gov/search.jsp?R=20190033315 (accessed June 6, 2020).

[3] Mital, Subodh, Robert Goldberg, and Peter Bonacuse. “Modeling of Damage Initiation and Progression in a SiC/SiC Woven Ceramic Matrix Composite.” In 53rd AIAA/ASME/ASCE/AHS/ASC Structures, Structural Dynamics and Materials Conference 20th AIAA/ASME/AHS Adaptive Structures Conference 14th AIAA, p.652. 2012..

[4] M.B. Goldsmith, B. V Sankar, R.T. Haftka, R.K. Goldberg, Effects of microstructural variability on thermo-mechanical properties of a woven ceramic matrix composite, J. Compos. Mater. 49 (2015) 335–350. https://doi.org/10.1177/0021998313519151.

[5] Gowayed, Y., Ojard, G., Prevost, E., Santhosh, U. and Jefferson, G., 2013. Defects in ceramic matrix composites and their impact on elastic properties. Composites Part B: Engineering, 55, pp.167-175. https://doi.org/10.1016/j.compositesb.2013.06.026

[6] Del Puglia, P., Sheikh, M.A. and Hayhurst, D.R., 2004. Classification and quantification of initial porosity in a CMC laminate. Composites Part A: Applied Science and Manufacturing, 35(2), pp.223-230. https://doi.org/10.1016/j.compositesa.2003.09.026

[7] Santhosh, U., Gowayed, Y., Ojard, G., Smyth, I., Kalarikkal, S. and Jefferson, G., 2018. Quantification of Porosity in Ceramic Matrix Composites Using Thermography. Journal of Nondestructive Evaluation, 37(2), p.37. https://doi.org/10.1007/s10921-018-0487-z

[8] Santhosh, U., Ahmad, J., Ojard, G., Smyth, I., Gowayed, Y. and Jefferson, G., 2020. Effect of porosity on the nonlinear and time-dependent behavior of Ceramic Matrix Composites. Composites Part B: Engineering, 184, p.107658. https://doi.org/10.1016/j.compositesb.2019.107658

[9] Borkowski, Luke, and Aditi Chattopadhyay. “Multiscale model of woven ceramic matrix composites considering manufacturing induced damage.” Composite Structures 126 (2015): 62-71.

[10] R.K. Goldberg, P.J. Bonacuse, Investigation of Effects of Material Architecture on the Elastic Response of a Woven Ceramic Matrix Composite, NASA/TM 2012-217269. (2012). http://www.sti.nasa.gov (accessed August 26, 2019).

[11] K.C. Liu, S.M. Arnold, Influence of scale specific features on the progressive damage of woven ceramic matrix composites (CMCs), Comput. Mater. Contin. 35 (2013) 35–65. http://www.techscience.com/doi/10.3970/cmc.2013.035.035.pdf (accessed August 5, 2019)

[12] K. Balusu, T. Skinner, A. Chattopadhyay, An efficient implementation of the high-fidelity generalized method of cells for complex microstructures, Comput. Mater. Sci. 186 (2021) 110004. https://doi.org/10.1016/j.commatsci.2020.110004

[13] K. H. Khafagy, S. Datta, and A. Chattopadhyay. “Multiscale Characterization and Representation of Variability in Ceramic Matrix Composites.” Journal of Composite Materials, 2020 (in press)

[14] J. Aboudi, M.J. Pindera, S.M. Arnold, Linear thermoelastic higher-order theory for periodic multiphase materials, J. Appl. Mech. Trans. ASME. 68 (2001) 697–707. https://doi.org/10.1115/1.1381005.

[15] Y. Bansal, M.-J. Pindera, Testing the Predictive Capability of the High-Fidelity Generalized Method of Cells Using an Efficient Reformulation, 2004. http://www.sti.nasa.gov (accessed January 27, 2020)

[16] Y. Bansal and M.-J. Pindera, Testing the Predictive Capability of the High-Fidelity Generalized Method of Cells Using an Efficient Reformulation, no. April 2004. 2004.

[17] Yang, C.P., Zhang, L., Wang, B., Huang, T. and Jiao, G.Q., 2017. Tensile behavior of 2D-C/SiC composites at elevated temperatures: Experiment and modeling. Journal of the European Ceramic Society, 37(4), pp.1281-1290. https://doi.org/10.1016/j.jeurceramsoc.2016.11.011.

[18] Daniel, I.M., Ishai, O., Daniel, I.M. and Daniel, I., 1994. Engineering mechanics of composite materials (Vol. 3, pp. 256-256). New York: Oxford university press.